PREPARED FOR THE U.S. DEPARTMENT OF ENERGY,
UNDER CONTRACT DE-AC02-76CH03073

PPPL-3810
UC-70

PPPL-3810

Confinement Studies of Auxiliary Heated NSTX Plasmas

by

B.P. LeBlanc, M.G. Bell, R.E. Bell, M.L. Bitter, C. Bourdelle, D.A. Gates,
S.M. Kaye, R. Maingi, J.E. Menard, D. Mueller, S.F. Paul, A.L. Roquemore,
A. Rosenberg, S.A. Sabbagh, D. Stutman, E.J. Synakowski, V.A. Soukhanovskii,
J.R. Wilson and the NSTX Research Team

May 2003

PPPL
PRINCETON PLASMA
PHYSICS LABORATORY

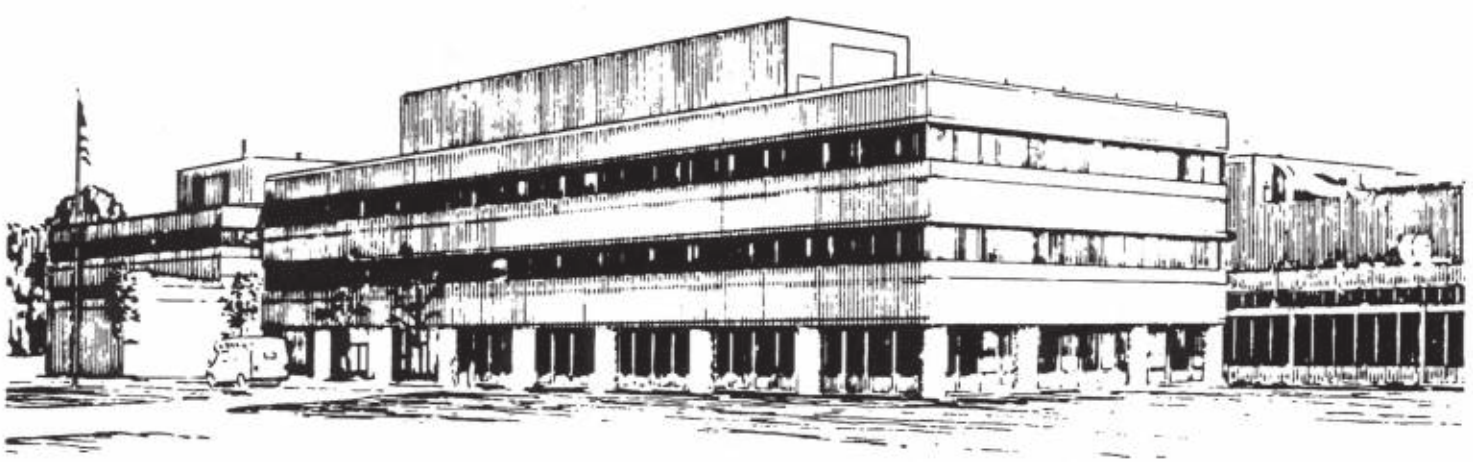

PRINCETON PLASMA PHYSICS LABORATORY
PRINCETON UNIVERSITY, PRINCETON, NEW JERSEY

PPPL Reports Disclaimer

Availability

This report is posted on the U.S. Department of Energy's Princeton Plasma Physics Laboratory Publications and Reports web site in Fiscal Year 2003. The home page for PPPL Reports and Publications is: http://www.pppl.gov/pub_report/

DOE and DOE Contractors can obtain copies of this report from:

U.S. Department of Energy
Office of Scientific and Technical Information
DOE Technical Information Services (DTIS)
P.O. Box 62
Oak Ridge, TN 37831

Telephone: (865) 576-8401

Fax: (865) 576-5728

Email: reports@adonis.osti.gov

This report is available to the general public from:

National Technical Information Service
U.S. Department of Commerce
5285 Port Royal Road
Springfield, VA 22161

Telephone: 1-800-553-6847 or
(703) 605-6000

Fax: (703) 321-8547

Internet: http://www.ntis.gov/ordering.htm

Confinement Studies of Auxiliary Heated NSTX Plasmas

B.P. LeBlanc[1], M.G. Bell[1], R.E. Bell[1], M.L. Bitter[1], C. Bourdelle[2], D.A. Gates[1], S.M. Kaye[1], R. Maingi[3], J.E. Menard[1], D. Mueller[1], S.F. Paul[1], A.L. Roquemore[1], A. Rosenberg[1], S.A. Sabbagh[4], D. Stutman[5], E.J. Synakowski[1], V.A. Soukhanovskii[1], J.R.Wilson[1] and the NSTX Research Team

[1] *Princeton Plasma Physics Laboratory, Princeton University, Princeton, New Jersey 08543*

[2] *DRFC, CEA, Cadarache, Saint-Paul lez Durance cedex, France*

[3] *Oak Ridge National Laboratory, Oak Ridge, Tennessee 37830*

[4] *Department of Applied Physics, Columbia University New York, New York 10027*

[5] *Johns Hopkins University, Baltimore, Maryland*

e-mail contact of main author: bleblanc@pppl.gov

Abstract: The confinement of auxiliary heated NSTX discharges is discussed. The energy confinement time in plasmas with either L-mode or H-mode edges is enhanced over the values given by the ITER97L and ITER98Pby(2) scalings, being up to 2-3 times L-mode and 1.5 times H-mode. TRANSP calculations based on the kinetic profile measurements reproduce the magnetics-based determination of stored energy and the measured neutron production rate. Power balance calculations reveal that, in a high power neutral beam heated H-mode discharge, the ion thermal transport is near neoclassical levels, and well below the electron thermal transport, which is the main loss channel. Perturbative impurity injection techniques indicate the particle diffusivity to be slightly above the neoclassical level in discharges with L-mode edge. High-harmonic fast-wave (HHFW) bulk electron heating is described and thermal transport is discussed. Thermal ion transport is found to be above neoclassical level, but thermal electron transport remains the main loss mechanism. Evidences of an electron thermal internal transport barrier obtained with HHFW heating are presented. A description of H-mode discharges obtained during HHFW heating is presented.

1 Introduction

The National Spherical Torus Experiment (NSTX) is a medium size spherical torus (ST) [1], which combines the advantages of plasma shaping with an intrinsic strong magnetic shear associated with low aspect ratio. The device produces plasmas with a nominal geometric center at major radius R_G = 0.85 m and minor radius a = 0.68 m, resulting in an aspect ratio of ≥ 1.27. The applied toroidal field at the center can be set within the 0.3-0.6 T range, and discharges with plasma current in the 0.3-1.5 MA range were produced. The device operates in inner-wall limited, single-null or double-null configurations, producing shaped plasmas with elongation $\kappa \leq 2.2$, and triangularly $\delta \leq 0.8$. So far NSTX has achieved, non-simultaneously, stored energies up to 0.39 MJ, energy confinement times τ_E < 0.12 s and $\beta_T \leq$ 35% [2], where β_T is defined as $\langle p \rangle / (B_0^2/2\mu_0)$, where <p> is the volume averaged total pressure and B_0 is the vacuum magnetic field at R_G. Auxiliary heating plays an important role in the research program [3], with deuterium neutral beam injection (NBI) power of up to 7 MW at injection energies between 60 and 100 keV, and high-harmonic fast-wave (HHFW) heating [4] with power up to 6 MW. A recent machine upgrade permits baking at 350° C, supplementing boronization [5] and helium glow to condition the first-wall surfaces, all of which were crucial to attaining high confinement reproducibility. H-mode access reproducibility is significantly enhanced with the use of center stack fueling [6].

This paper gives an assessment of global confinement and local transport during auxiliary heating in NSTX. In Sec. 2, we compare NSTX energy confinement times against two conventional aspect ratio scalings. In Sec. 3, we describe the NSTX kinetic profile data set. In Sec. 4, we discuss thermal confinement in a high power NBI heated H-mode discharge. Section 5 presents results from perturbative measurements of the particle diffusivity in an

NBI heated L-mode discharge. Section 6 describes bulk electron heating by HHFW and discusses thermal transport in these plasmas. In Sec. 7, we comment on some of the properties of H-mode plasmas obtained with HHFW heating. A discussion is presented in Sec. 8, which is followed by a conclusion.

2. Global Confinement Scaling

The global confinement in NSTX is noticeably good, easily comparable to that of tokamaks of similar size whose toroidal fields are significantly larger, which augurs well for the ST concept. In Fig. 1(a) we show the experimental energy confinement time of NBI heated discharges plotted against the value determined from the L-mode scaling ITER97L [7]. The experimental energy confinement times are global (i.e. containing the fast-ion stored energy without subtraction of the fast-ion losses) and were determined from the EFIT [8,9] magnetic reconstruction of the NSTX plasmas. Except for the two plasmas indicated by dashed circles, the discharges shown have achieved a non-transient phase lasting two confinement times. H-mode plasmas are indicated by circles, while L-mode edge plasmas are shown with triangles. In Fig. 1(b) we present a similar plot for the thermal scaling ITER98Pby(2) [10] H-mode scaling, still using the global experimental values for comparison. We see that the L-mode edge plasmas in NSTX can achieve comparatively good or equivalent confinement as the H-mode plasmas. The NSTX data lay above both scalings, being up to 1.5 times H-mode and between two and three times L-mode. One should add here that a fraction of the stored energy is contained in the non-thermal ions ($\approx 25 - 30$ %), and that the fast-ion losses are quite dependent on the neutral density and plasma current respectively. We are presently in the process of correcting the data with the fast ion effects.

3. Kinetic Profile Measurements

A concerted effort has been made to put on line and validate baseline kinetic profile diagnostics. We can see in Fig. 2 a top view of NSTX, showing some of the diagnostics – and elements of the NBI and HHFW auxiliary heating systems. The Thomson scattering diagnostic [11] provides measurements of the electron density and temperature profiles, $n_e(R,t)$ and $T_e(R,t)$, with a nominal time resolution of 17 ms (2 x 30 Hz) and utilizes 20 spatial channels in its current configuration. Here "*R*" stands for major radius. Charge exchange recombination spectroscopy (CHERS) provides measurements of the ion temperature and toroidal velocity profiles, $T_i(R,t)$ and $v_\phi(R,t)$ of the intrinsic carbon impurity. There are 17 spatial channels covering the outer half of the plasma and the time resolution is 20 ms. The radiated power $P_{rad}(R,t)$ is obtained from a 16-chord bolometer array. Four 16-channel soft x-ray (SXR) cameras are in operation. One limitation remains, for the moment, that we do not have a routine profile measurement of Z-effective, and we typically have to rely on a single chordal measurement which gives a time history of the line-average Z-effective, although profile information can be obtained from the SXR data. Details about the NSTX diagnostic data set can be found elsewhere [12].

Examples of kinetic profiles are shown in Fig. 3, where we see in the top panel an overlay of the experimental T_i and T_e profiles obtained during a high power (6 MW) H-mode discharge. A good match between T_i and T_e is seen in the edge region, as to be expected in this collisional region of the plasma. A substantial difference is observed in the central region, where T_i =1.9 keV while T_e = 1.1 keV. The bottom panel shows the corresponding toroidal velocity profile, where we see that v_ϕ reaches ≈ 210 km/s in the core region. This is a

relatively fast rotation for NSTX, with M_A = 0.26 where $M_A = v_\phi / v_A$ and v_A is the Alfvén velocity.

The availability of profile and temporal information permits to use the TRANSP [13] code to pursue a kinetically based analysis of a discharge and to investigate local transport through power and momentum balance calculations. TRANSP uses Monte-Carlo calculations of the neutral beam power deposition and fast-ion slowing down, which permit to compute the energy stored in the supra thermal particles and the neutron production rate. One way to judge the validity of the kinetic profile data is by comparing TRANSP predictions for global parameters like the total stored energy and the neutron production rate to independent measurements. In Fig. 4(a) we show an overlay of the – kinetically based – TRANSP time dependant estimate of the stored energy compared to the – magnetically derived – estimate from EFIT. The good match seen throughout the time evolution indicates global agreement between magnetic and kinetic estimates of the stored energy. One also sees in Fig. 4(a) that the fast-ion stored energy fraction decreases with time, being of the order of 20% of the total energy at the end of the discharge. A similar comparison for the neutron production rate is shown in Fig. 4(b). The TRANSP estimate is compared to fission-chamber measurement. Large scale MHD activity developes in this discharge after 0.48 sec. The discrepancy between the measured and calculated neutron signal after this time indicates that fast ions are either expelled or redistributed by the MHD. This loss/redistribution has not yet been modeled, but the agreement between the TRANSP and EFIT calculated stored energies through the MHD active period, along with the neutron signal discrepancies, will set a bound on the magnitude of this effect.

4. Thermal Transport during NBI Heating

The overall agreement between global measurements and TRANSP predictions gives credence to the kinetic data set and the TRANSP analysis itself. We now move from global to local scale and investigate thermal transport. Figure 5 displays four time evolution panels for a deuterium high power NBI heated discharge lasting beyond 0.55 s. In the top panel we see that the flattop of the 0.9 MA plasma current starts at 0.18 s. The plasma has a lower single null configuration (LSN) for the time of interest. Three neutral beam sources are staggered with respective onset times of 0.1, 0.2 and 0.25 s; NBI lasts until the end of the discharge. The injection energy ranges from 80 keV to 95 keV. β_T reaches 15% and the energy confinement time, τ_E, is ≈ 0.04 s. A vertical dotted line marks the H-mode transition time, which can be seen on the D_α trace (bottom panel). The central ion temperature, T_{i0}, and electron temperature,T_{e0}, are equal during the early phase of auxiliary heating. But for times greater than 0.22 s, T_{i0} increases over T_{e0} and remains greater until the end of the discharge. A small drop of T_{io} at ≈ 0.42 s is echoed by T_{e0}. The $T_i(R)$, $T_e(R)$ and $v_\phi(R)$ profiles shown in Fig. 3 correspond to $t = 0.45$ s of this discharge. Since the NBI system uses beam energy typically many times larger than the 1-2 keV electron temperature, one would expect from classical slowing down physics of fast particles that most (≈ 2/3) of the neutral beam power be deposited into the electron population. The experimental observation that T_i is greater than T_e during NBI despite the expected preferential electron heating suggests that the ion confinement is much better than that of the electrons. The third panel shows global measurements stored energy and neutron production rate. The comparison between TRANSP predictions and global measurements in Fig. 4 corresponds to the experimental data shown in this panel. The effects of the H mode are seen in the bottom panel where the central density, n_{e0} and the volume average density $\langle n_e \rangle$ are displayed. One sees that $n_{e0} \approx \langle n_e \rangle$ from 0.25s

to 0.40 s, corresponding to a phase where $n_e(R)$ profile builds up "ears" in the edge regions. A similar observation is made on MAST [14]. Later on n_{e0} becomes greater than $<n_e>$ as the center of the density profile fills in. This behavior can be seen in Fig 6, which shows $n_e(R)$ profiles at selected times throughout the discharge duration. Keeping these observations in mind and remembering the decreasing fast-ion content shown in Fig. 4, we observe a progressive thermalization of the injected fast particles into a thermal plasma that maintains fairly constant central temperatures T_{i0} and T_{e0}, while the density increases continuously until the end of the discharge. More details about H-mode plasmas in NSTX can be found elsewhere [15].

Figure 7 shows profiles of the power and momentum balance diffusivities extracted from TRANSP analysis at t = 0.45 s. The momentum diffusivity χ_ϕ is the lowest in magnitude, hovering slightly below 1 m^2/s in the core region and increases towards the edge up to slightly higher than 2 m^2/s. The χ_i profile has a different behavior, being the largest in the core region and lowest in the edge region. The neoclassical χ_i^{NC} prediction from the NCLASS code [16] follows the shape of χ_i over the whole profile. This is partially due to the fact that χ_i^{NC} is computed using the neoclassical ion thermal flux from NCLASS and the measured local gradient and density. One notes that $\chi_i \approx \chi_i^{NC}$ in the core region, while $\chi_i < \chi_i^{NC}$ in the outer region. The electron thermal confinement is poor, with large χ_e values reflecting the flattening of the core T_e profile seen in Fig. 3. The overall $\chi_e(R)$ shape is also unusual, being lower at the edge than at in the core. These results support the inference that the ion confinement is superior to that of the electrons in NSTX NBI discharges. Microinstability analysis using the gyrokinetic code GS2 [17], shows the high beta gradient to have a strong stabilizing impact on the drift waves in NSTX [18], which could explain ITG growth rates lower than ExB shearing rates. On the other hand high T_i/T_e ratio favors ion drift waves stability and electron drift wave instability, which might explain the large electron transport.

5. Perturbative Measurement of Particle Transport in NBI Heated Plasma

The ion particle transport can be probed in experiments where small amount of neon ($n_{neon}/ne \approx 0.5\%$) is injected for 20 msec in L-mode edge plasmas. Radiation emitted from the peripheral and core charge states is measured simultaneously using two ultra soft x-ray diode cameras [19] fitted with Be foil filters having respectively 0.6 keV and 1.4 keV cutoff energy. The local emissivity is obtained by inverting the SXR signals, and is displayed in Fig. 8 for the two energy ranges. The radiation from the lower neon charge states range is emitted from the peripheral region following the gas puff, while essentially no radiation comes from the core region. Only when an MHD reconnection occurs at $t \approx 0.26$ s, does the peripheral radiation collapse and radiation is emitted from the core region, indicating that neon does not penetrate beyond $r/a \approx 0.5$-0.6 (before MHD). By modeling the instrumental emission and making use of the MIST impurity transport code [20], a particle diffusivity can be determined, which is found to be slightly higher than the NCLASS neoclassical expectation for low-Z impurities in the extended core area. Further details will be found elsewhere [21].

6. HHFW Heated Plasmas

HHFW heating is an important auxiliary heating system that complements NBI. The antenna array comprises 12 current carrying elements driven by transmitters operating at 30 MHz. The elements are located vertically side-by-side in an array that occupies one quarter of the outer midplane periphery. Driving juxtaposed elements in opposite phase generates a nominally balanced launch spectrum with $k_{//} = \pm 14$ m^{-1}, but for readability we will refer to it

as $k_{//} = 14$ m^{-1}. Although other launch spectra can be produced, only $k_{//} = 14$ m^{-1} launch is discussed here. The frequency of operation is 30 MHz.

The application of HHFW power is an effective means of bulk electrons heating. One can see in Fig. 9 the temporal evolution of relevant plasma parameters of a LSN helium discharge undergoing HHFW heating. The toroidal field is 0.45 T and the plasma current 0.8 MA. HHFW power reaching 3.3 MW is applied during the 0.1-0.26 s time interval. One can see that following the HHFW power onset, a rapid increase of the central electron temperature, T_{e0}, raising from 0.3 keV to 1.3 keV in 0.06 s. β_T reaches 4.5% and $\tau_E \approx 0.014$ s. The low T_{e0} seen at $t \approx 0.045$ s is caused by a radial shift of the plasma column. Two NBI short pulses were injected to measure the T_i profile by charge exchange recombination spectroscopy. Figure 10 shows an overlay of the T_i and T_e profiles corresponding to the second beam blip. We find again good agreement between T_i and T_e in the edge region. In the central region, T_e reaches 1.4 keV, while T_i remains at 0.8 keV, as one would expect under this condition of electron heating.

A TRANSP analysis can be made by making use of the HPRT[22] code for the computation of the HHFW power deposition by ray tracing. Figure 11 shows the result of such a calculation for a time within the second NBI diagnostic pulse. Most of the HHFW power is absorbed by the electrons, P_e. The power absorption occurs over a wide profile, but peaks at the center. Only a very small amount of power is computed to be absorbed by the thermal ions, P_{He}. We also see that during NBI, some HHFW power is absorbed by the fast ions, P_{FI}. Since the power absorbed by the fast ions will eventually trickle down to the thermal plasma, we have ad hoc divided P_{FI} evenly between thermal ions and electrons for the present TRANSP analysis. Globally, the computed power going to the thermal ions is ≤ 10% of that going to the electrons. In absence of NBI, the electrons absorb essentially all the HHFW power. One can see in Fig. 12 profiles of the thermal diffusivities at t =0.243 s corresponding

to the time shown in Fig. 10. Contrary to what was seen in the pure NBI case shown earlier on, one sees that $\chi_i > \chi_i^{NC}$. Electron thermal transport remains the leading loss mechanism. The thermal diffusivities χ_i and χ_e bare profiles that are lower at the center and larger near the edge.

Under certain conditions, high central T_e is achieved, nearing 4 keV with a behavior reminiscent of an internal transport barrier. We can see in Fig. 13 successive $T_e(R)$ and $n_e(R)$ profiles for a deuterium plasma heated with 2.5 MW of HHFW power. This LSN discharge has a plasma current of 0.8 MA and a toroidal field of 0.45 T. The line-average Z-effective increases during during the time of interest from 3.0 to 4.5. Soft x-ray measurements indicate the Z effective profile to be centrally peaked. The HHFW power onset occurs at 0.1 s and six Thomson scattering times are shown spanning interval 0.127 to 0.210 s, during which HHFW is applied. During this interval, one can see a rapid central T_e increase from below 1 keV to measured value ≤ 3.9 keV. On the other hand there is little change in the density profile, although the last two times show a shift and a narrowing of the $n_e(R)$ profile. Bearing in mind the limited spatial resolution of this – 10-channel – earlier configuration of the Thomson scattering diagnostic, the behavior seen here suggests the presence of an electron thermal internal transport barrier, with a foot at $r/a \approx 1/2$. We can see in Fig. 14 an overlay of the time evolution of T_{e0} and the central ion temperature T_{i0} from a x-ray crystal spectrometer [23]. We see that as T_{e0} increases to nearly 4 keV, T_{i0} also increases, with some delay, to 2 keV. A MHD reconnection occurs at 0.22 s. In Fig. 15 we show results from a TRANSP analysis for this plasma. For this analysis, $T_i(R,t)$ is assumed to have the same profile shape as $T_e(R,t)$, but is scaled according to measured T_{i0} . Power deposition is computed with HPRT. Because of the limitations of procedure used to obtain $T_i(R)$, only the core values of χ_e are shown. The five times shown correspond to those seen in Fig. 13 to within 2 ms. It is interesting to note that while $T_e(R,t)$ progressively peaks spatially in the core region, the associated χ_e(R,t)

profile decreases to values in the range of 1-3 m^2/s. These behaviors are suggestive of an electron thermal internal transport barrier. Another indication of a change in confinement is the observed accumulation of impurity in the core region. A small peaking of the electron density profile for the last two Thomson scattering time points (Fig. 13) also suggests a change in the particle confinement, although this effect is small.

7. HHFW Driven H-mode Discharges

Transitions into the H-mode are observed during HHFW heating in LSN discharges and the relevant parameters for such a deuterium discharge are shown in Fig. 16. The plasma current is 0.36 MA, and the magnetic field is 0.45 T. HHFW power of 3.3 MW is applied during interval 0.12-0.32 s. The HHFW frequency is 30 MHz with $k_{//}$ = 14 m^{-1}. T_{e0} rapidly responds to the HHFW power by increasing from 0.3 keV to nearly 1.5 keV in 0.05 s. The H transition occurred at 0.195 s and was accompanied by further heating of the electrons and an increase in the stored energy. The decrease in central electron temperature observed later on probably resulted from power-coupling losses caused by MHD activity or the ELMs (visible on the D_α trace). TRANSP analysis predicts a 40% bootstrap current fraction for this discharge. On some occasions, peaked electron temperatures can be maintained during the ELM activity as illustrated in Fig.17. In this case, T_e remained above 1.5 keV for 0.1 s, including times of ELM activity. A smaller outer gap might explain the better behavior of this discharge, but more work is needed to determine optimal power coupling requirements.

Kinetic profiles of HHFW driven H-mode plasma show the expected signatures of this high confinement regime. In Fig. 18, we show $T_e(R)$ and $n_e(R)$ profiles for a deuterium discharge with HHFW power applied at 0.2 s. The H-mode phase occurred during the interval 0.235-0.285 s. The four times points shown – 0.193, 0.227, 0.243, 0.277 s –

correspond respectively to the ohmic phase, the L phase, the early and late H phases. They are respectively marked OH, L, H1 and H2. During the ohmic phase, the T_e profile is flat and limited to 0.3 keV; the density profile is peaked. During the L phase, we observe a T_e increase over the whole profile with the center reaching 1.1 keV; the density profile change from peaked to triangular shape. There is a hint of a edge profile steepening visible on $T_e(R)$ and $n_e(R)$ outboard data. The early H-mode $n_e(R)$ data show a well established edge gradient. The plasma column has shifted inwards by ≈ 3 cm and the electron temperature is slightly increased. The temperature edge pedestal is ≈ 0.12 keV. During the later H-mode phase, we observe a fully developed edge density gradient with "ears" near the peripheral regions. Meanwhile the central electron temperature has fallen to 0.6 keV.

8. Discussion

NSTX NBI heated plasmas have good global confinement with performances better than L-mode and H-mode ITER scaling predictions ITER97L and ITER98Pby(2). A word of caution should be added, since we use these scaling relations out of their interpolation range by going to low aspect ratio, where their validity has not been verified so far. Global measurements stored energy and the neutron production rate are supported by kinetic profile diagnostic data, which reproduce their time evolution, when used in conjunction with the TRANSP code. Although NSTX diagnostics are relatively new, this temporal agreement for global measurements suggests the kinetic data to be in good order in a global sense. In the previous sections, we have used these analysis and diagnostic tools to study transport in plasmas heated with two different auxiliary power techniques, which are theoretically expected to heat electrons predominately.

Experimental observations agree with theoretical expectation during HHFW heating. We observe a strong electron heating and $T_e > T_i$. Looking at the helium discharge and considering the 80% of the plasma width excluding the immediate core and edge, we find that $1 < \chi_i / \chi_i^{NC} < 6$, where the lower limit corresponds to the inner region and the higher limit corresponds to outer region. χ_e is ≈ 10 times greater at the edge that in the core. But χ_e can fall to as low as ≈ 3 m^2/s during the formation of an ITB (deuterium discharge). The best electron thermal confinement occurs in the central region.

The results are different with NBI heating. While the theory predicts most of the power to heat the electrons, it is observed that $T_i > T_e$. One may surmise that an anomalous process may be draining the power off the electrons and the ion thermal confinement is very good. Indeed it is found that χ_i is at neoclassical level or lower over a wide range of the plasma column. Looking at the 80% of the plasma column excluding the immediate core and edge regions, we find that $0.5 < \chi_i / \chi_i^{NC} < 2$. Theses observations appear consistent with ion thermal transport being at or near neoclassical level. On the other hand χ_e is quite large and in excess of a minimum of 4 m^2/s located at the edge. While it is conceivable that χ_i be greater in the core than at the edge when the ion transport is nearing neoclassical level, it is more intriguing to obtain a χ_e profile with its minimum at the edge, since we know the electron transport to be far above neoclassical.

Seeing these "inverted" χ_i and χ_e profiles, one might worry about experimental error. While we saw above that the kinetic profile data set reproduces well the global parameters, it is conceivable that more subtle experimental issues might play a role. But we also know that the same diagnostic set was also used in the analysis of the HHFW heated discharges, where inverted χ_i and χ_e profiles were not obtained. With the caveat of an unresolved diagnostic or analysis error occurring during NBI, our present observation is that of inverted thermal diffusivity profiles during with NBI, but not with HHFW. This unusual behavior might hide

unidentified physics not included in the TRANSP computation of the thermalization of the fast NBI ions. These effects would distort the TRANSP χ_e and χ_i profiles, but would have a lesser effect on the χ_ϕ profile, which does not show signs of inversion. An anomalous ion heating mechanism has been proposed, which might provide an explanation [24]. Also a mechanism for an enhanced – over neoclassical –heat pinch has been proposed for NBI heated plasmas [25], which might help elucidate the differing transport observations in NBI and HHFW plasmas. Bearing in mind that the neon gas puffing analysis presented here is done on different NBI plasmas, we find that the particle diffusivity is slightly higher than neoclassical in the core region of L-mode discharges.

That the thermal confinement of the NBI discharge is globally better than that of the HHFW plasma can be visualized in the respective χ_e and χ_i profiles. While the local maxima of χ_e and χ_i are of the same magnitude for the NBI and HHFW plasmas, they occur at different radial positions. In the NBI case, confinement is poor in the core region, but improves towards the peripheral region. The opposite is true for the HHFW case and the largest thermal diffusivities are found in the outer half of the plasma. Because of volume effects, the latter condition has a deleterious effect on the global confinement.

HHFW heating provides a second mode means of accessing the H mode besides NBI. While HHFW H-mode plasmas have lower stored energy than with NBI, they do have the expected kinetic profile signatures. Keeping in mind that, contrary to NBI, HHFW does not fuel and is not expected to impel torque, it should be revealing to compare these two modes of H-mode entry in order to study the physics of the transition on NSTX. The HHFW H-mode plasmas are also interesting since they could be used as target for HHFW current drive. The combination of bootstrap current and HHFW driven current is an attractive candidate to extend the duration of NSTX plasmas.

Electron thermal transport constitutes the main power loss channel during auxiliary heating in NSTX. This might not be too surprising in a magnetic device with such a low field and high β, where electromagnetic fluctuations will naturally play a more important role that in a tokamak. The observation of an electron thermal internal transport barrier during HHFW heating might bring some elements to a solution. Analysis suggest that ETG or TEM modes may be driving the electron transport. While full gyrokinetic analysis is not available, one may note that three effects might have contributed to stabilization in this case: (1) We have forced $T_e/T_i > 1$ by using HHFW; (2) The presence of impurity is also stabilizing; (3) While a local q profile diagnostic is not yet available, TRANSP calculations indicate a reversed q profile, which has a strong stabilizing effect on turbulence. Repeating this experiment under better impurity influx control would help us identify the preponderant stabilizing mechanism(s). Hence HHFW heating and reversed q profile operation, which are part of the research agenda, might provide tools to reduce the electron thermal transport.

Conclusion

We presented an assessment of the confinement behavior during auxiliary heated NSTX discharges. A crosscheck between global and kinetic profile diagnostics has been verified using the TRANSP code. Local analysis reveals the ions to be better confined that the electrons, with χ_i^{NC} nearing or lower than neoclassical predictions during NBI. But some unaccounted effects might be causing the – power balance derived – uncharacteristically low edge thermal transport relative to the core. Perturbative experiments indicate the particle transport to be slightly above the neoclassical expectations over the extended core region of L-mode edge plasmas. HHFW provides an effective way to heat electrons. Thermal transport is dominated by the electrons, and χ_i is a few times χ_i^{NC}. HHFW heating has been used to generated H-mode plasmas and discharges with behavior indicative of the generation of an electron thermal transport barrier. This work is supported by U.S. DOE contract DE-AC02-76CH03073.

[1] Peng Y.-K., Phys. Plasmas 7, 1681(2000)

[2] Menard J.E. et al, paper IAEA-CN-94/EX/S1-5 at this conference.

[3] D. Mueller *et al.,* IEEE transactions on Plasma Science, Vol 31, No. 1, pp. 60-67, (2003)

[4] Wilson, J.R. *et al.*, Phys. Plasmas, Vol. 10, No. 5, (2003) 1733-1738

[5] Skinner C.H., et al. Nucl. Fusion **42**, (2002) 329.

[6] Maingi, R. *et al.*, Plasma Phys. Control. Fusion **45** (2003) 657–669

[7] Kaye S.M. and the ITER Confinement Database Working Group, Nucl. Fusion, **37** (1997) 1303

[8] Sabbagh S.A., Kaye S.M., Menard J., et al., Nuclear Fusion 41 (2001) 1601.

[9] Lao, L., Nuc. Fusion 25 (1985) 1611

[10] ITER Physics, Nucl. Fusion, **39** (1999), 2175

[11] LeBlanc B.P., Bell R.E., Johnson D.W., *et al* , Rev. Sci. Instrum., Vol 74, No 3, pp 1659-1662, (2003).

[12] Johnson D.W. et al., German-Polish EURO-Conference on Plasma Diagnostics for Fusion and Applications, Greifswald, Germany, September 4-6, 2002

[13] Ongena J., Evrard M., McCune D., "Numerical Transport Codes", in the Proceedings of the Third Carolus Magnus Summer School on Plasma Physics, (Spa, Belgium, Sept 1997), as published in Transactions of Fusion Technology, March, 1998, Vol. 33, No. 2T, pp. 181-191.

[14] Sykes, A *et al.*, Phys. Plasmas. 8 (2001) 2101

[15] Maingi, R, *et al.*, "H-mode Research in NSTX" submitted to Nuclear Fusion.

[16] Houlberg, W.A., Shaing K.C., Hirshman S.P., Zarnstorff M.C., Phys. Plasmas 4, 3230 (1997)

[17] Kotschenreuther M, Rewoldt G.and W.M. Tang W.M, Computer Phys. Com. 88, 128 (1995).

[18] Bourdelle C. *et al.*, Phys. of Plasmas, to be published 2003

[19] Stutman D., Finkenthal M, Bourdelle C. *et al*, Proc. of 29th Euro. Conf. on Plasma Physics and Contr. Fusion, Montreux, Switzerland, June, 2002, paper P4.067.

[20] Hulse R.A., Nuclear Technology/Science 3, 259 (1983)

[21] Stutman D. *et al.*, in preparation

[22] Menard J., Majeski R., Kaita R., Ono M., Munsat T., Phys. Plasmas, **6** (1999) 2002.

[23] Bitter M, Hill K.W., Roquemore A.L., Beiersdorfer P., Kahn S.M., Elliot S.R., and Frankel B.,

Rev. Sci. Instrum **70**, 292 (1999)

[24] Gates D.A., Gorelenkov N.N., White R.B., Phys. Rev. Lett., **87**, 205003-1

[25] Hinton F.L., and Kim Y.-B., Phys. Fluids B 5 (1993) 3012

Figure captions

Figure 1: Energy confinement against ITER database scalings ITER97L (a) and ITER98Pby(2) (b). Data correspond to steady state discharges except for two plasmas indicated with dashed circle.

Figure 2: Top view of NSTX showing some of the kinetic profiles diagnostics and auxiliary NBI and HHFW heating systems.

Figure 3: Kinetic profile during NBI. (a) Overlay of T_e and T_i profiles. (b) Profile of v_ϕ . The the Alfvén Mach number reaches M_A = 0.26 in the plasma core.

Figure 4: (a) Temporal overlay of the measured stored energy and TRANSP estimate. TRANSP reproduces well the measured stored energy; (b): Temporal overlay of the measured neutron rate and TRANSP estimate. TRANSP reproduces well the measured DD neutron.

Figure 5: Time evolution of a high power NBI heated discharge. H-mode transition time is marked with a vertical dotted line.

Figure 6: Profiles of the electron density at different times during the NBI H-mode discharge. Individual times 0.2, 0.25, 0.3, 0.35, 0.4, 0.45, and 0.5 s are indicated. Time point 0.2 s corresponds to the L-mode phase. The density profile show “ear” in the edge region during the earlier NBI. Later on the plasma center fills in.

Figure 7: Experimental thermal diffusivity profiles against minor radius *r* during high power NBI heating: electron thermal, χ_e, ion thermal, χ_i, and momentum, χ_ϕ. Neoclassical calculation of ion thermal diffusivity, χ_i^{NC}.

Figure 8: Local emissivity reconstruction against time for the two USRX energy ranges. Radiation is contained to within the peripheral region until MHD reconnection.

Figure 9: HHFW heating in 0.5 MA, 0.45 T, He plasma. T_{e0} rises rapidly 1o 1.3 keV in response to HHFW power onset. Two short NBI pulse are use for T_i measurement.

Figure 10: Measured T_e and T_i profiles during second NBI diagnostic pulse. T_e is roughly twice T_i in core region. $T_e \approx T_i$ in edge region.

Figure 11: HHFW power deposition profiles from HPRT against minor radius *r*. Power absorbed by the electrons, P_e, the thermal ions, P_{He}, and the fast ions, P_{FI}.

Figure 12: Experimental thermal diffusivity profiles against minor radius *r* during HHFW heating: electron thermal, χ_e, and ion thermal, χ_i . Neoclassical calculation of ion thermal diffusivity, χ_i^{NC} .

Figure 13: Temporal overlays of T_e(R), and n_e(R) for at HHFW heated discharge. Six time points spanning 0.127 to 0.210 s. Central Te increases from below 1 keV to ≤ 3.9 keV; ne(R) is shifted and narrowed for last two times.

Figure 14: Central temperatures Ti0 and Te0 against time. Ti0 from x-ray crystal spectrometer. Horizontal bars on Ti0 data correspond to integration times. Te0 reaches 3.9 keV , while Ti0 reaches 2 keV.

Figure 15: TRANSP analysis for ITB discharge. χ_e profiles at 6 times, from 0.125 s to 0.210 s during the Te increase. In the core region χ_e , progressively decreases by a factor of 10 down to (3 m2/s, corresponding to the maximum measured Te of 3.9 keV.

Figure 16: Time evolution of an HHFW driven H-mode discharge. In response of to the HHFW pulse Te0 increases rapidly. The transition is seen at 0.195 s on the D_ trace; stored energy WMHD doubles. A drop in Te0 occurs during the ELM activity.

Figure 17: Time evolution of an HHFW driven H-mode discharge. In response of to the HHFW pulse T_{e0} increases rapidly. The transition is seen at 0.165 s on the D_α trace. High T_{e0} is maintained during the ELM activity and stored energy increases more than twofold.

Figure 18: Temporal overlays of $T_e(R)$, and $n_e(R)$ for a HHFW driven H-mode discharge. Four times are shown: ohmic (OH), L-mode (L), early H-mode (H1), late H-mode (H2).

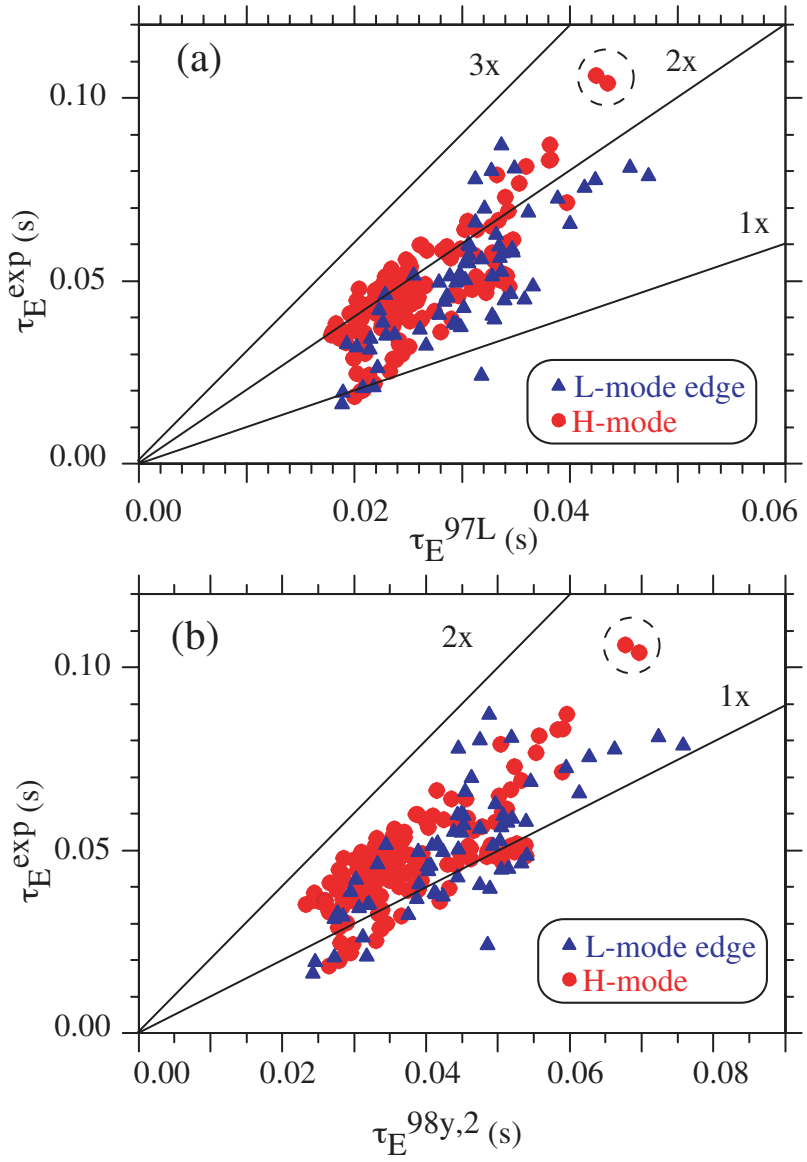
(a)
3x
2x
1x
0.10
0.05
0.00
τ_E^{exp} (s)
L-mode edge
H-mode
0.00
0.02
0.04
0.06
τ_E^{97L} (s)
(b)
2x
1x
0.10
0.05
0.00
τ_E^{exp} (s)
L-mode edge
H-mode
0.00
0.02
0.04
0.06
0.08
$\tau_E^{98y,2}$ (s)

Fig. 1

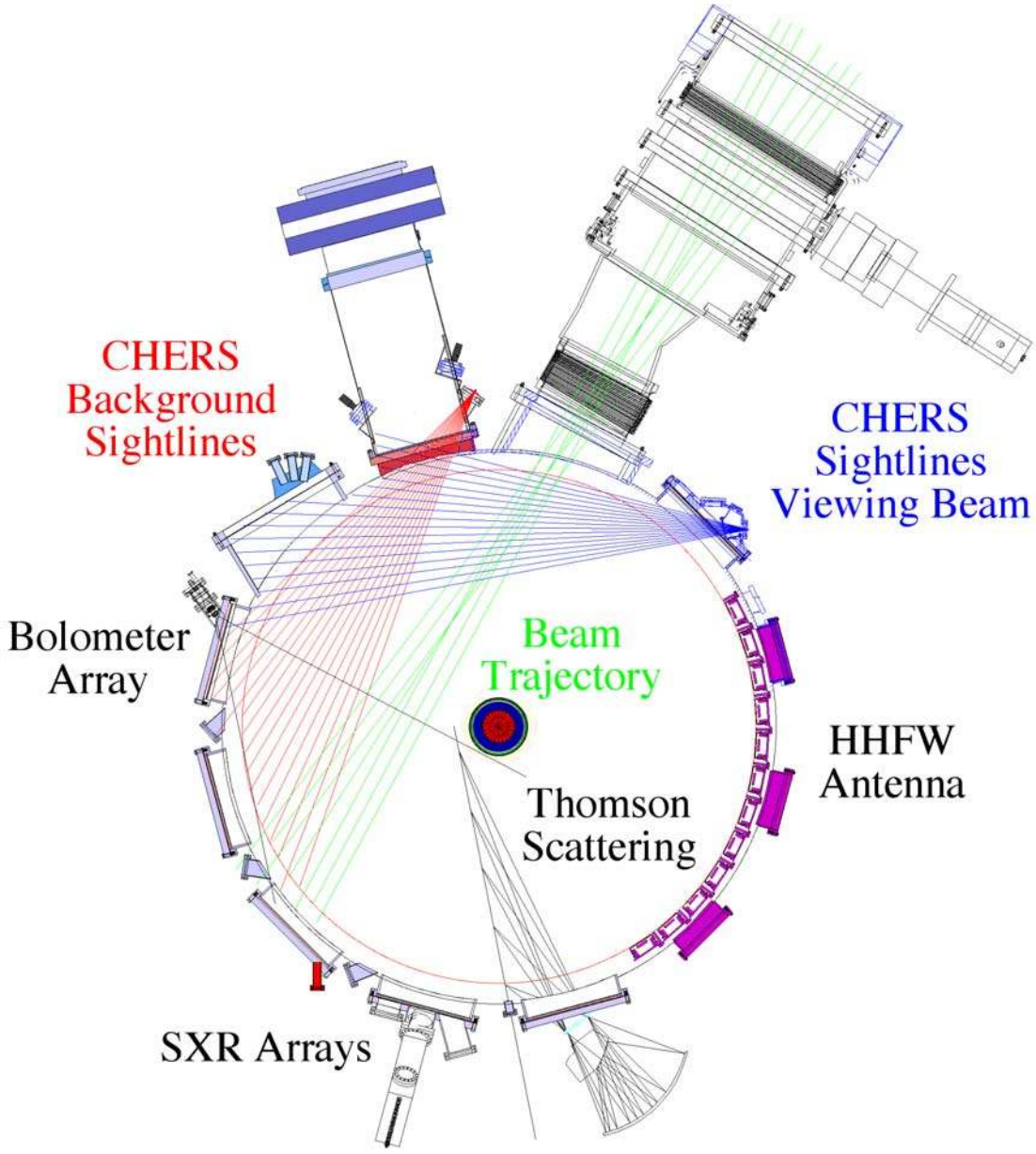

Fig. 2

NSTX_DIAG.TIFF

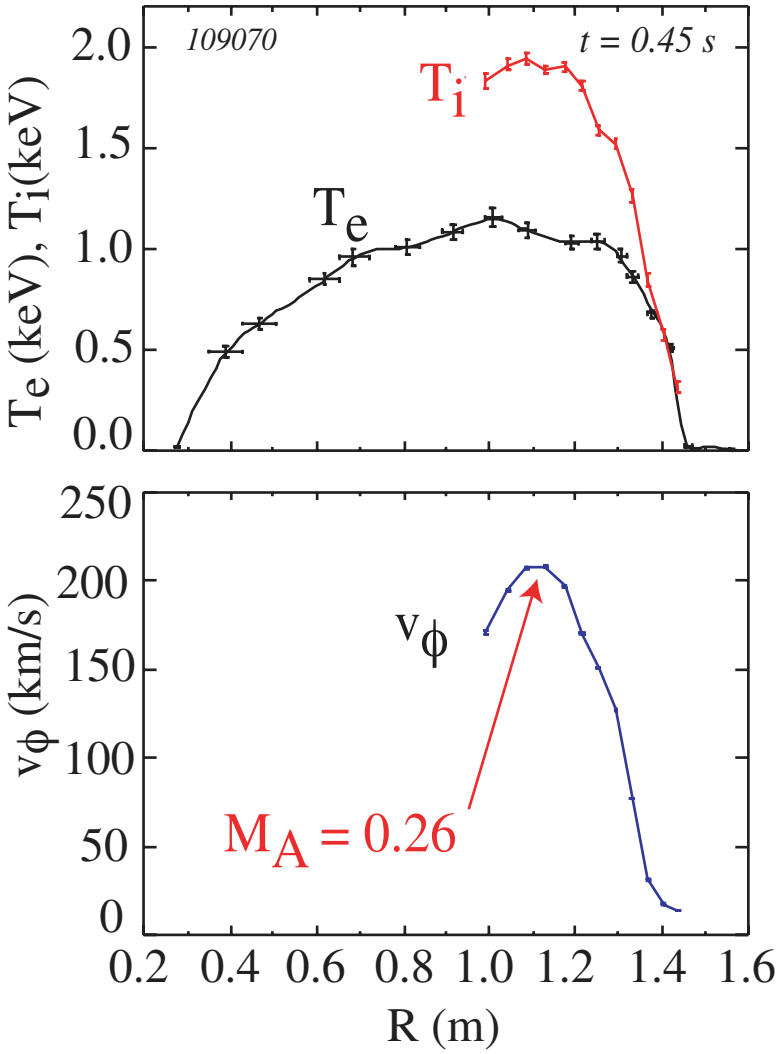
109070
t = 0.45 s
T_i
T_e
T_e (keV), T_i(keV)
2.0
1.5
1.0
0.5
0.0
250
200
150
100
50
0
vϕ (km/s)
vϕ
$M_A = 0.26$
0.2
0.4
0.6
0.8
1.0
1.2
1.4
1.6
R (m)

Fig. 3

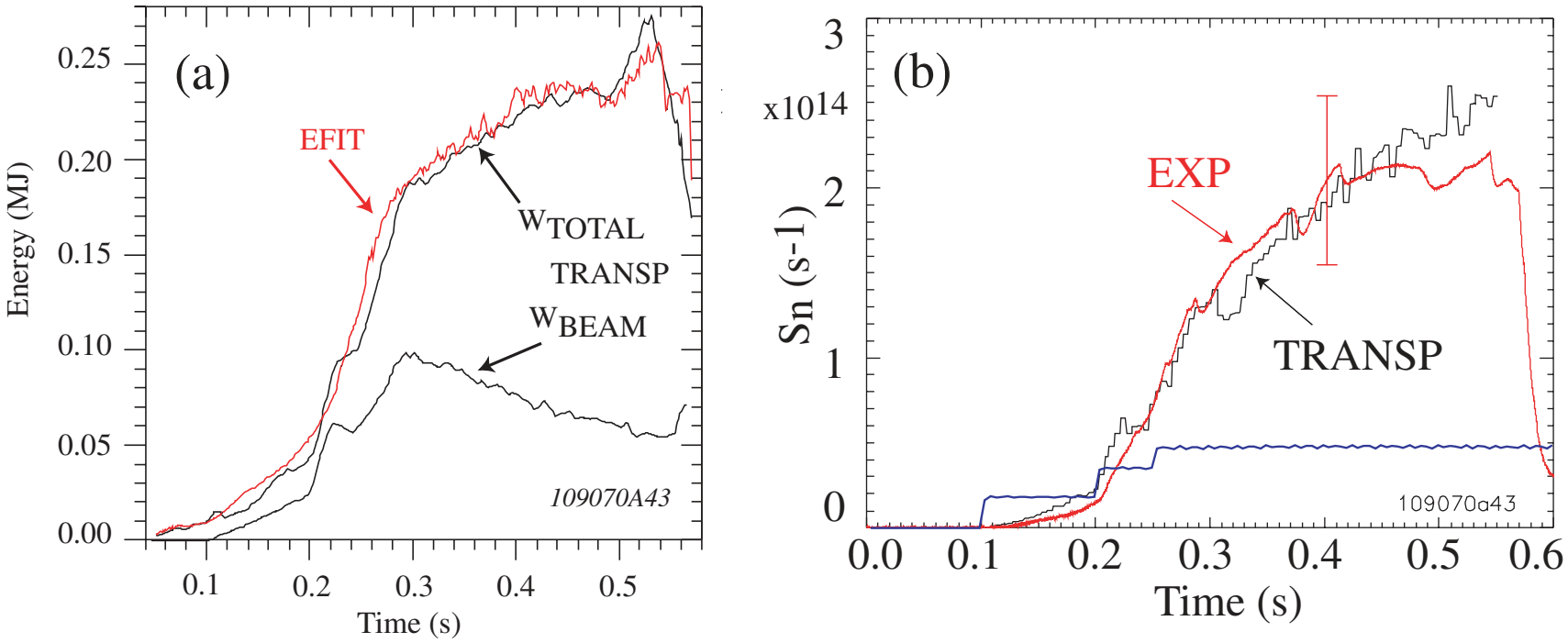
(a)
EFIT
W TOTAL
TRANSP
W BEAM
109070A43
Energy (MJ)
0.25
0.20
0.15
0.10
0.05
0.00
0.1
0.2
0.3
0.4
0.5
Time (s)
(b)
x10 14
EXP
TRANSP
109070a43
Sn (s-1)
3
2
1
0
0.0
0.1
0.2
0.3
0.4
0.5
0.6
Time (s)

Fig. 4

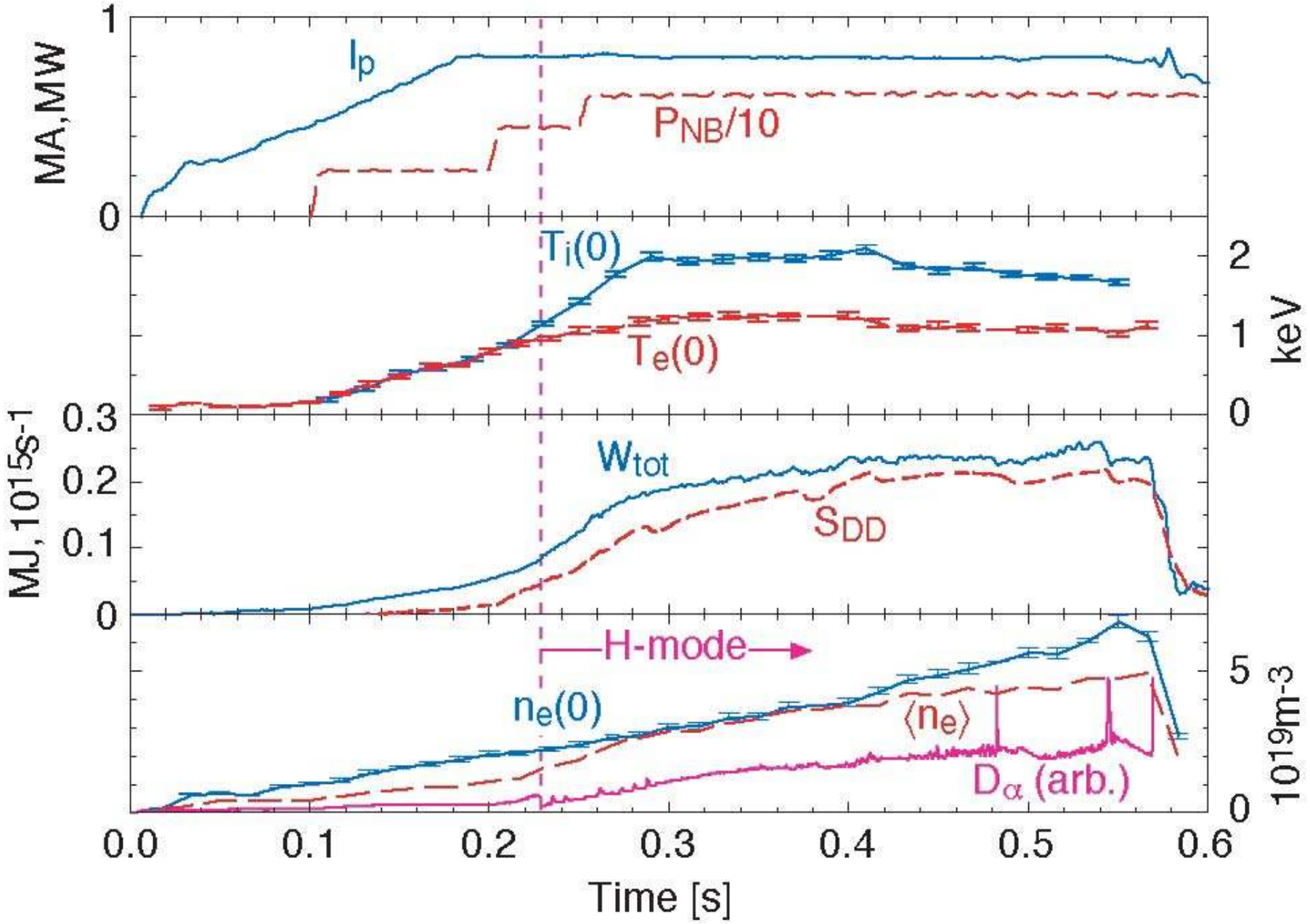
MA,MW
1
0
I_p
$P_{NB}/10$
$T_i(0)$
$T_e(0)$
2
1
0
keV
MJ,10^{15}s^{-1}
0.3
0.2
0.1
0
W_{tot}
S_{DD}
H-mode
$n_e(0)$
$\langle n_e \rangle$
D_α (arb.)
5
0
10^{19}m^{-3}
0.0
0.1
0.2
0.3
0.4
0.5
0.6
Time [s]

Fig. 5

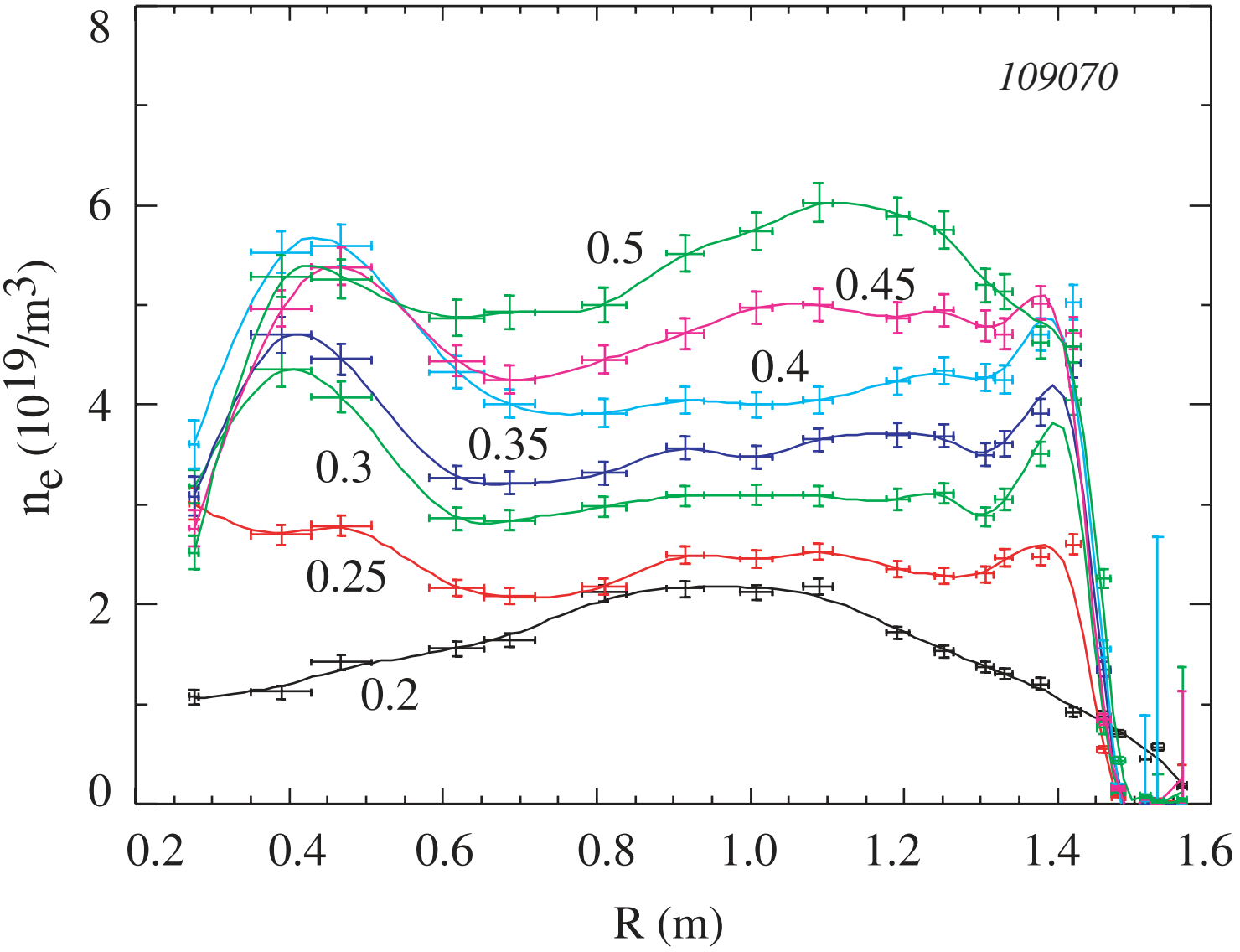
109070
0.5
0.45
0.4
0.35
0.3
0.25
0.2
n_e (10^{19}/m^3)
R (m)
0
2
4
6
8
0.2
0.4
0.6
0.8
1.0
1.2
1.4
1.6

Fig. 6

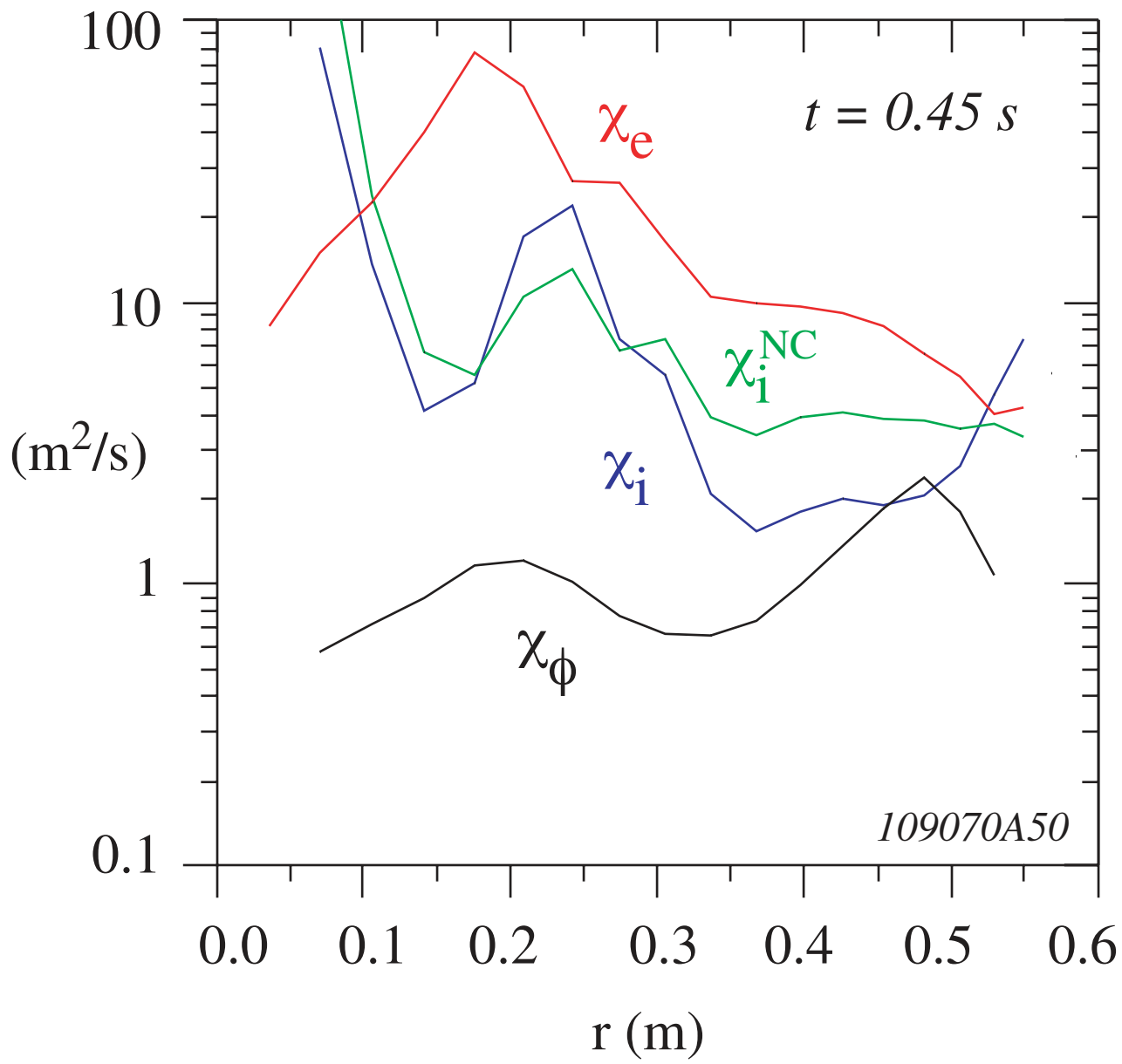
100
10
1
0.1
(m²/s)
χe
t = 0.45 s
χiNC
χi
χφ
109070A50
0.0
0.1
0.2
0.3
0.4
0.5
0.6
r (m)

Fig. 7

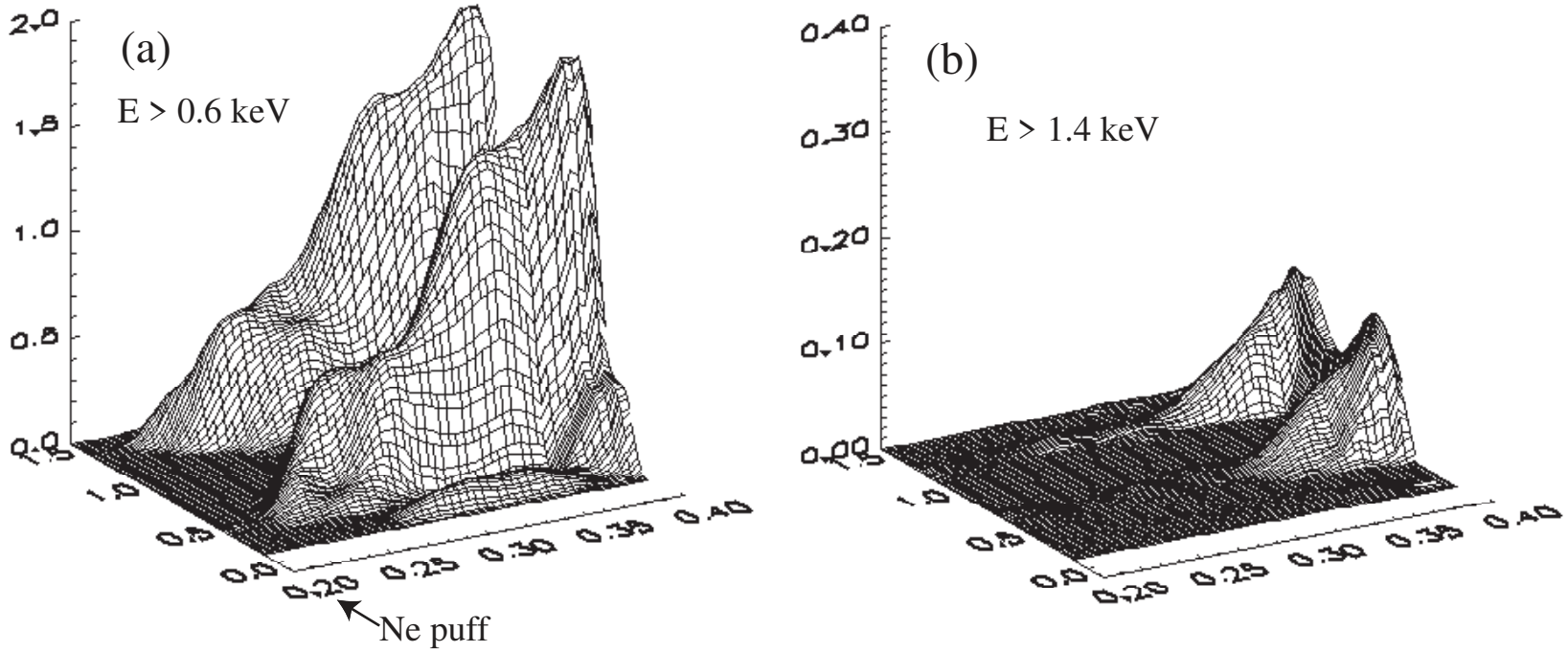
(a)
E > 0.6 keV
2.0
1.5
1.0
0.5
0.0
1.0
0.75
0.50
0.20
0.25
0.30
0.35
0.40
Ne puff
(b)
E > 1.4 keV
0.40
0.30
0.20
0.10
0.00
1.0
0.75
0.50
0.20
0.25
0.30
0.35
0.40

Fig. 8

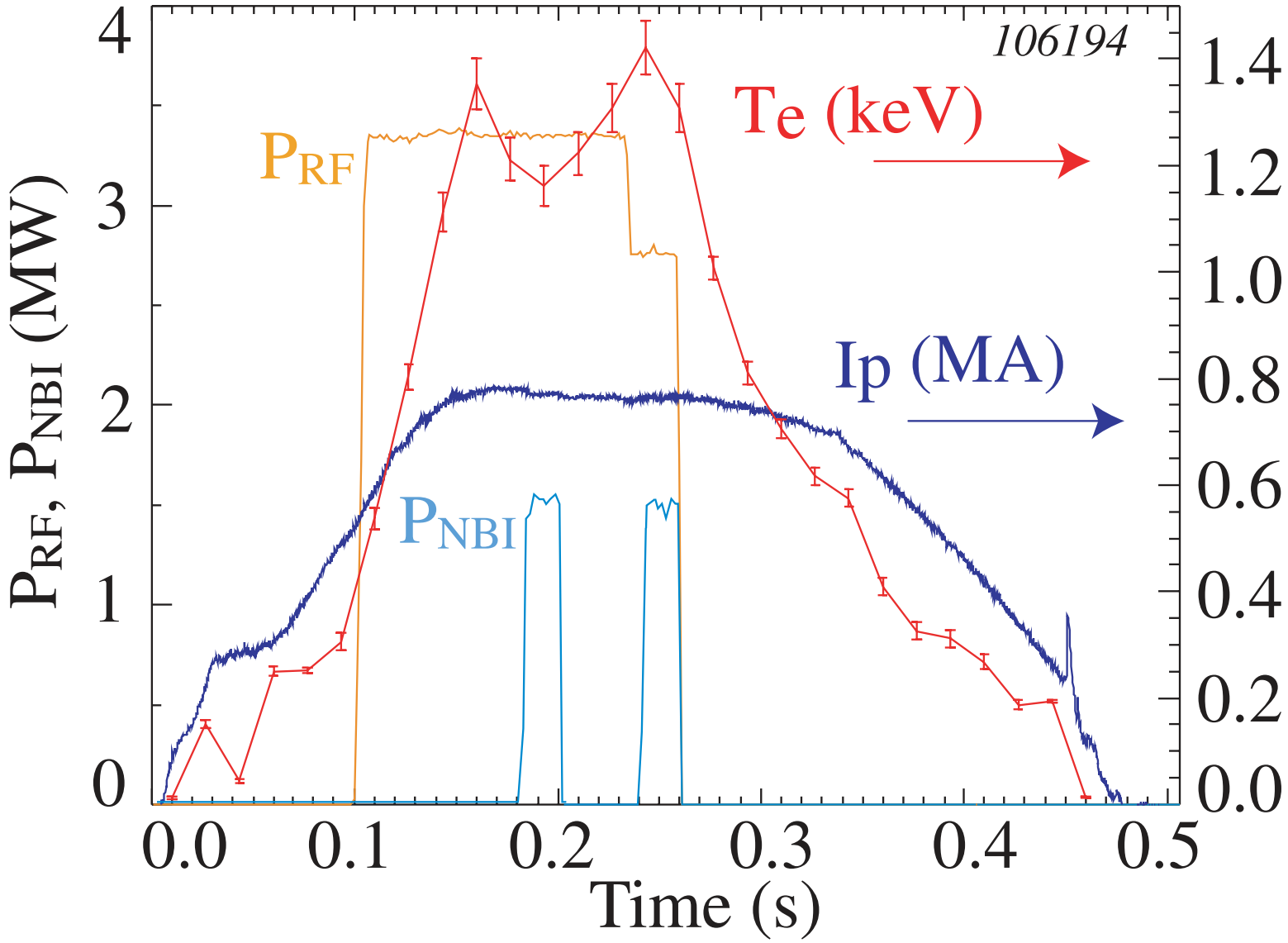
106194
Te (keV)
Ip (MA)
PRF
PNBI
PRF, PNBI (MW)
Time (s)
0
1
2
3
4
0.0
0.2
0.4
0.6
0.8
1.0
1.2
1.4
0.0
0.1
0.2
0.3
0.4
0.5

Fig. 9

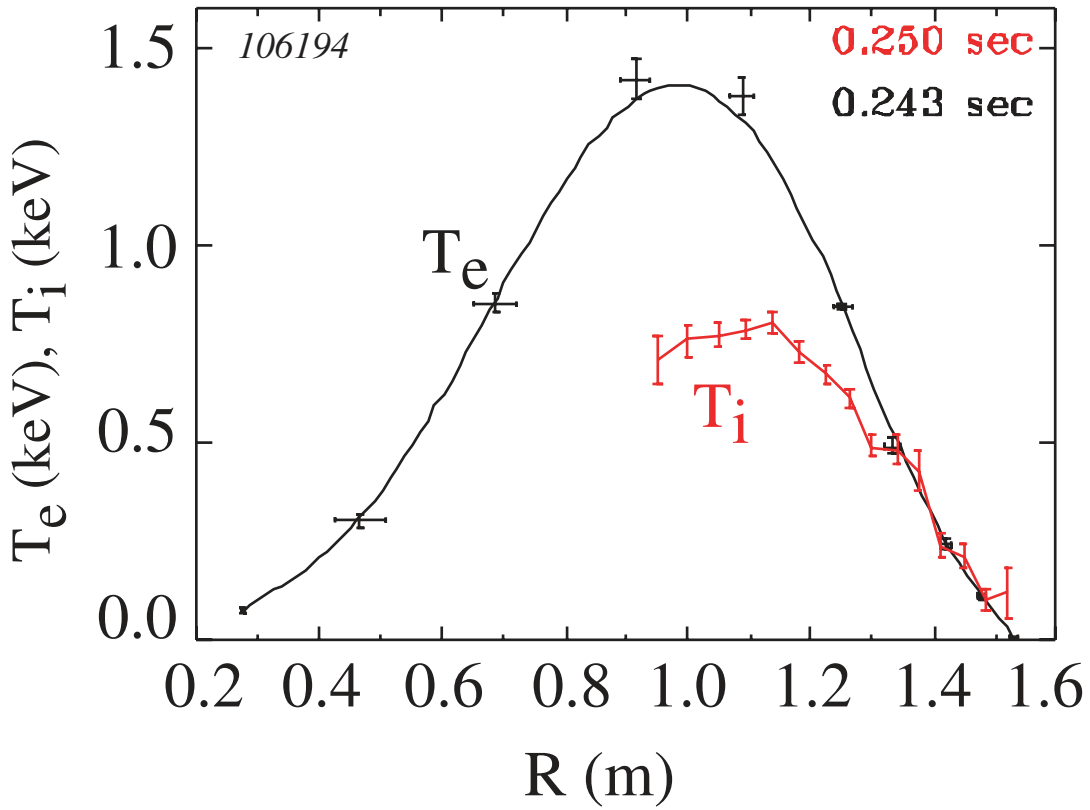
106194
0.250 sec
0.243 sec
T_e
T_i
T_e (keV), T_i (keV)
R (m)
0.0
0.5
1.0
1.5
0.2
0.4
0.6
0.8
1.0
1.2
1.4
1.6

Fig. 10

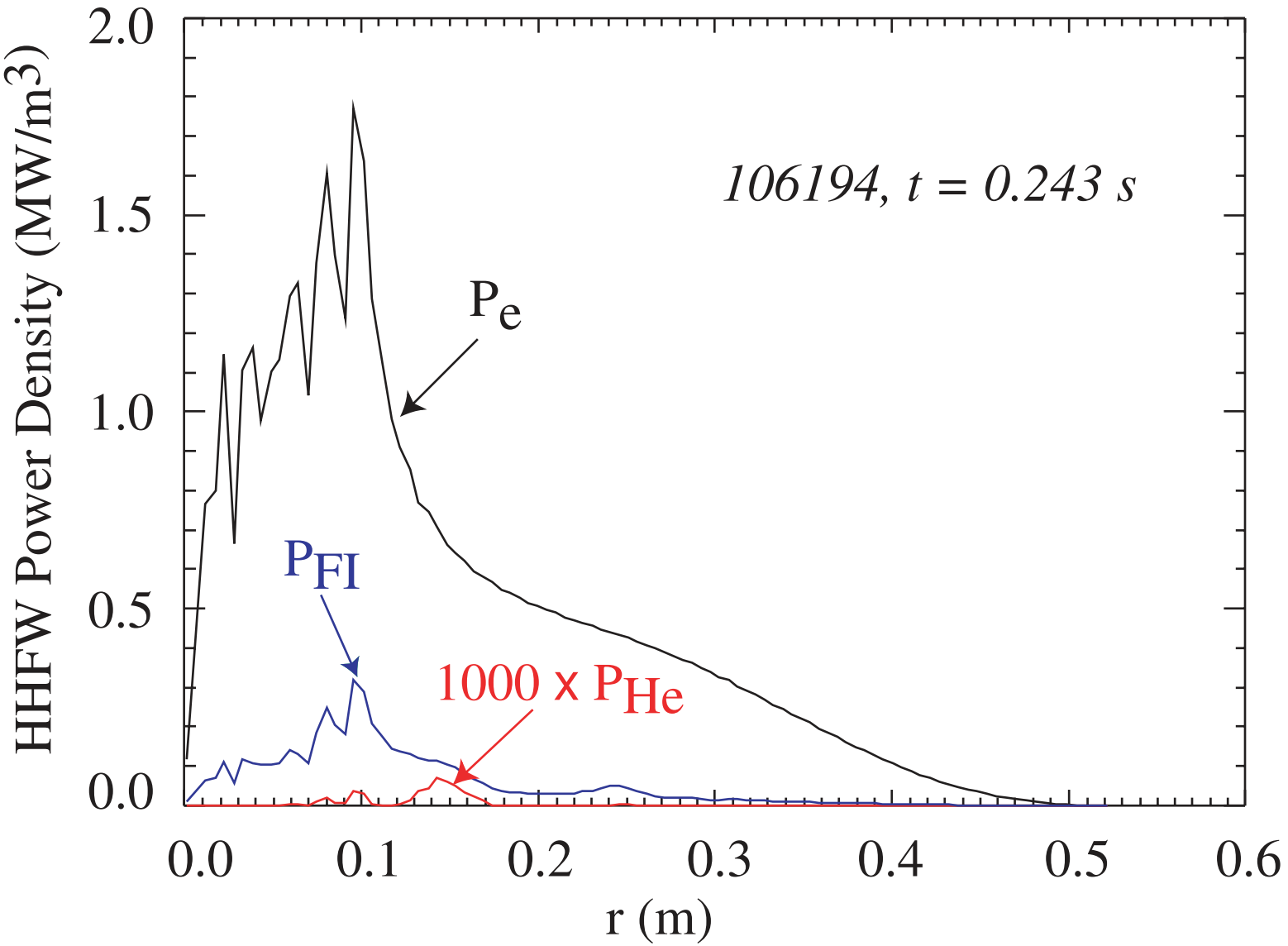
2.0
1.5
1.0
0.5
0.0
HHFW Power Density (MW/m3)
106194, t = 0.243 s
Pe
PFI
1000 x PHe
0.0
0.1
0.2
0.3
0.4
0.5
0.6
r (m)

Fig. 11

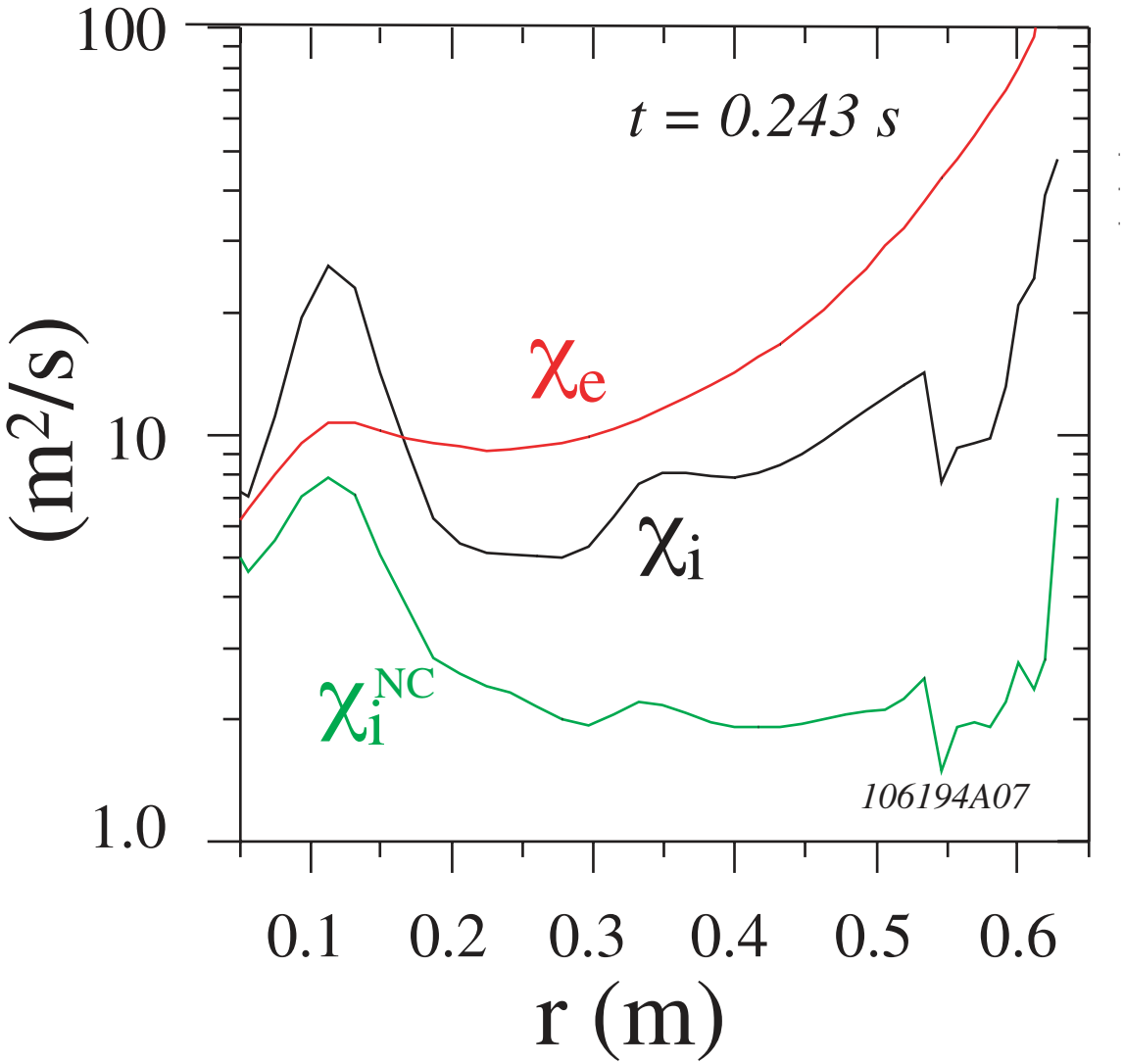

Fig. 12

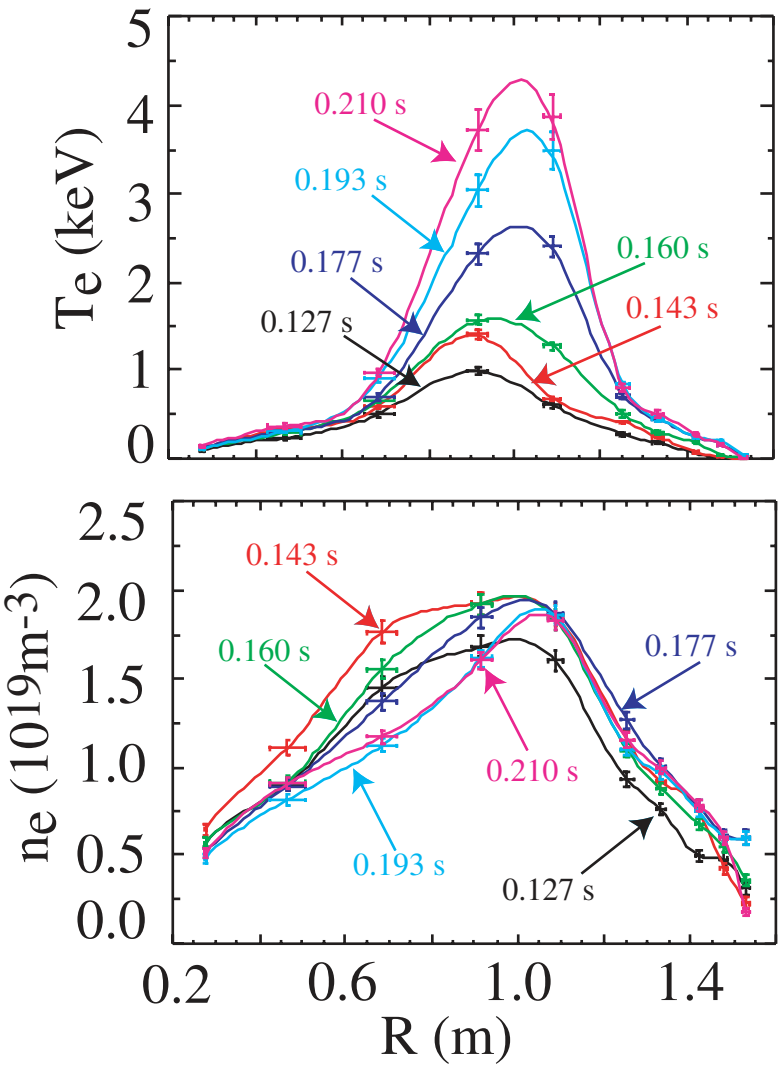
Te (keV)
0.210 s
0.193 s
0.177 s
0.160 s
0.143 s
0.127 s
ne (1019m-3)
0.143 s
0.160 s
0.177 s
0.210 s
0.193 s
0.127 s
R (m)

Fig. 13

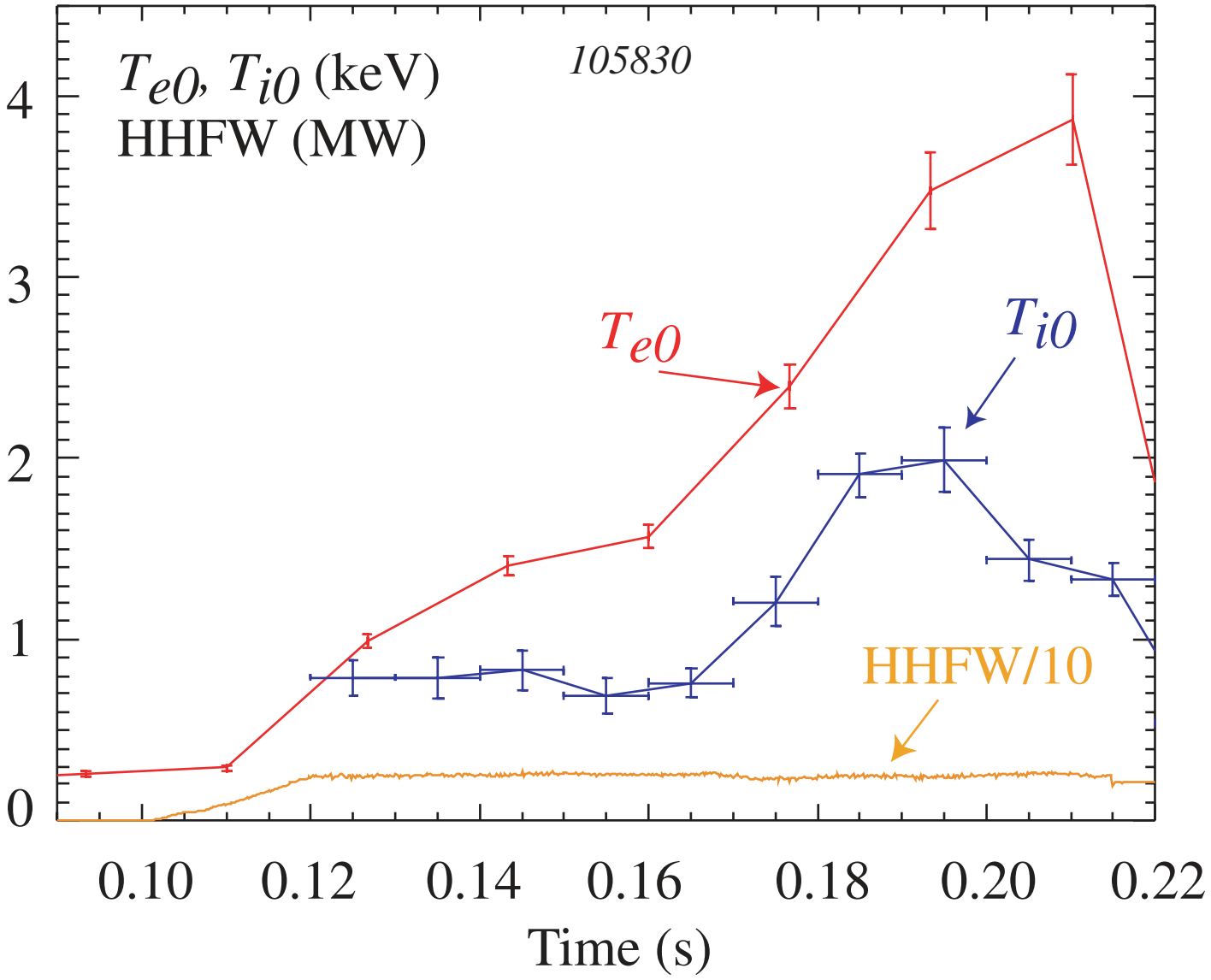
T_{e0}, T_{i0} (keV)
HHFW (MW)
105830
T_{e0}
T_{i0}
HHFW/10
0
1
2
3
4
0.10
0.12
0.14
0.16
0.18
0.20
0.22
Time (s)

Fig. 14

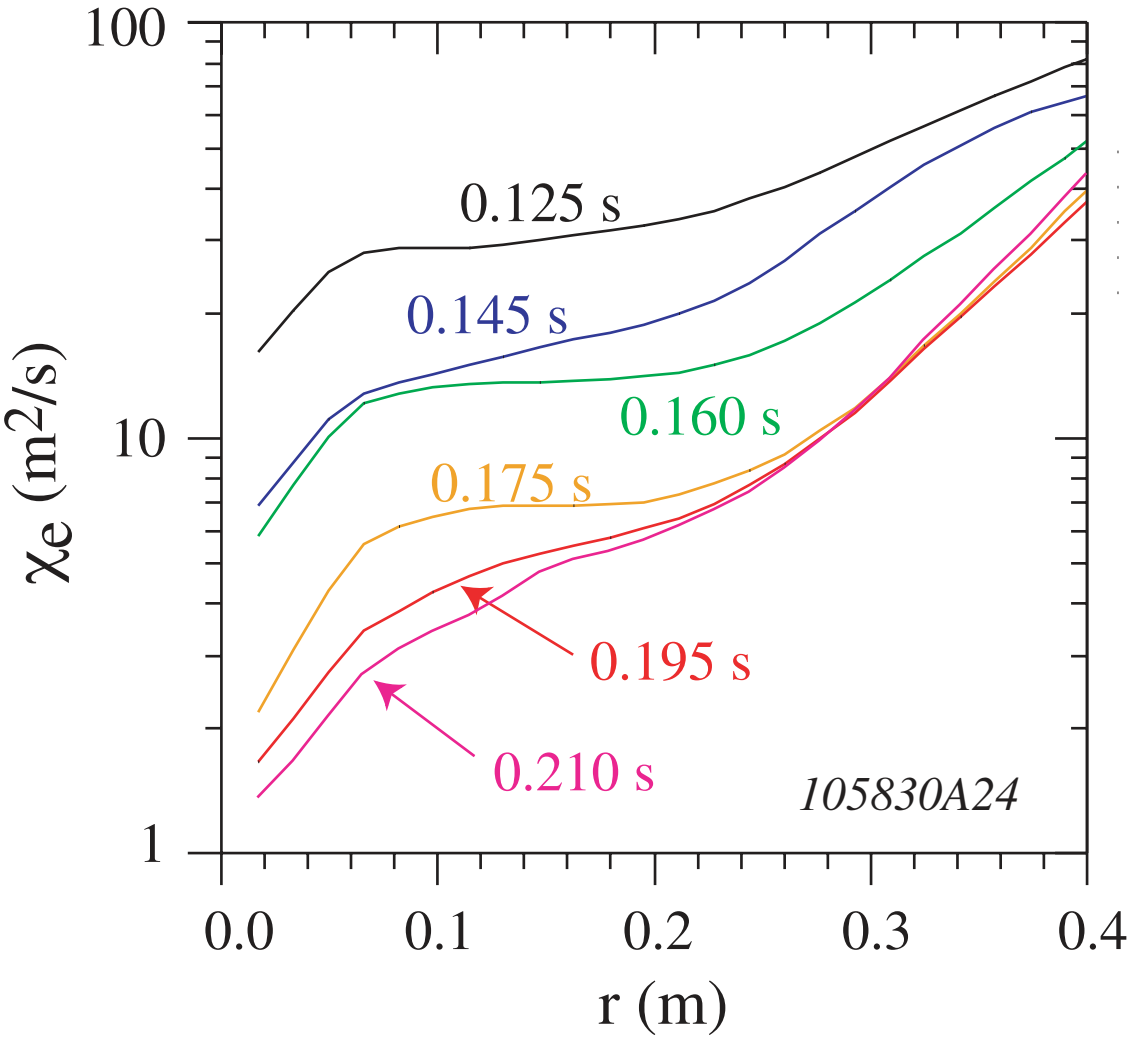
100
10
1
0.0
0.1
0.2
0.3
0.4
r (m)
χe (m2/s)
0.125 s
0.145 s
0.160 s
0.175 s
0.195 s
0.210 s
105830A24

Fig. 15

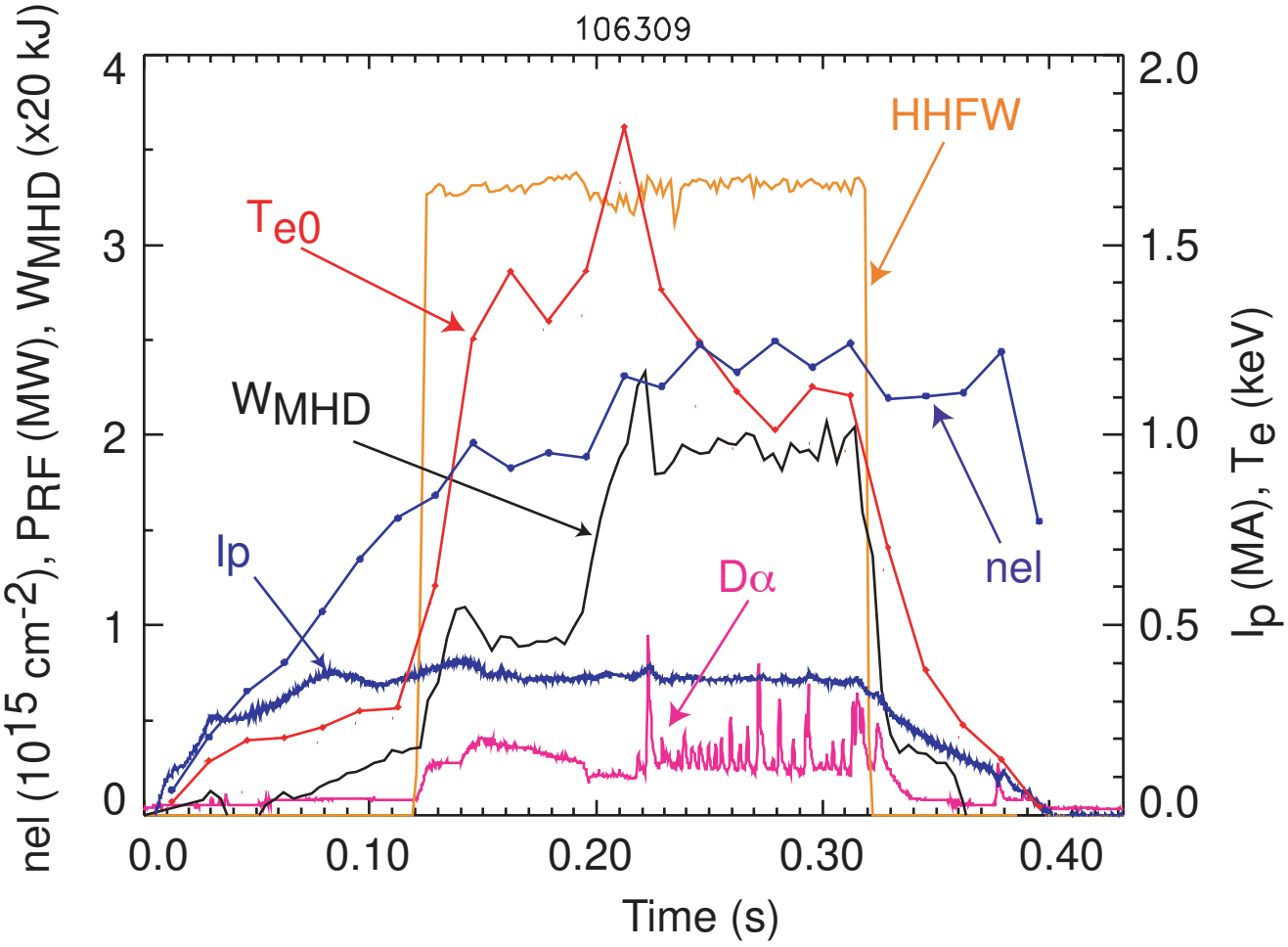
106309
HHFW
T_{e0}
W_{MHD}
Ip
Dα
nel
nel (10^{15} cm^{-2}), P_{RF} (MW), W_{MHD} (x20 kJ)
I_p (MA), T_e (keV)
Time (s)
0.0
0.10
0.20
0.30
0.40
0
1
2
3
4
0.0
0.5
1.0
1.5
2.0

Fig. 16

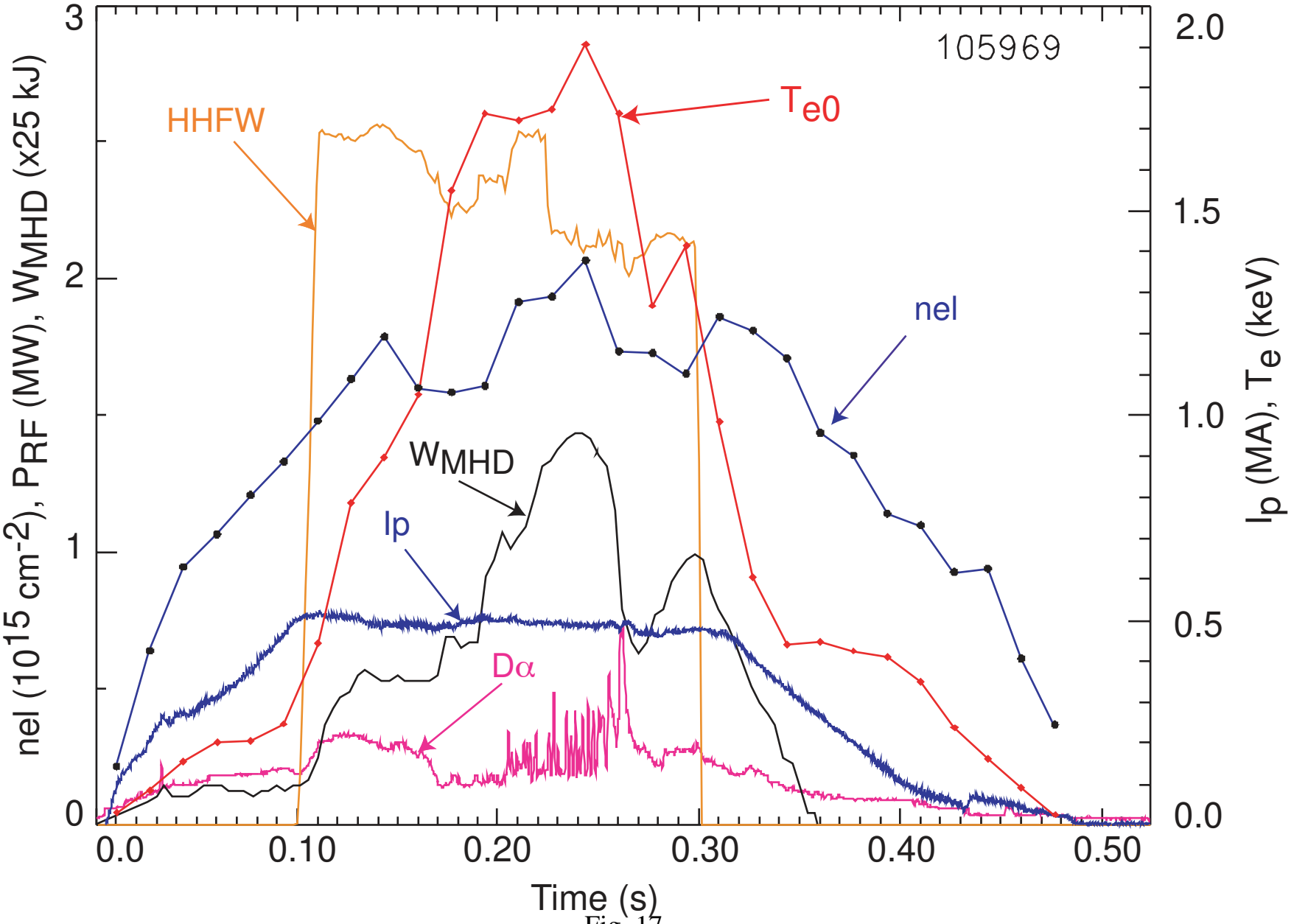
105969
HHFW
T_{e0}
nel
W_{MHD}
Ip
Dα
nel (10^{15} cm^{-2}), P_{RF} (MW), W_{MHD} (x25 kJ)
I_p (MA), T_e (keV)
Time (s)
0.0
0.10
0.20
0.30
0.40
0.50
0
1
2
3
0.0
0.5
1.0
1.5
2.0

Fig. 17

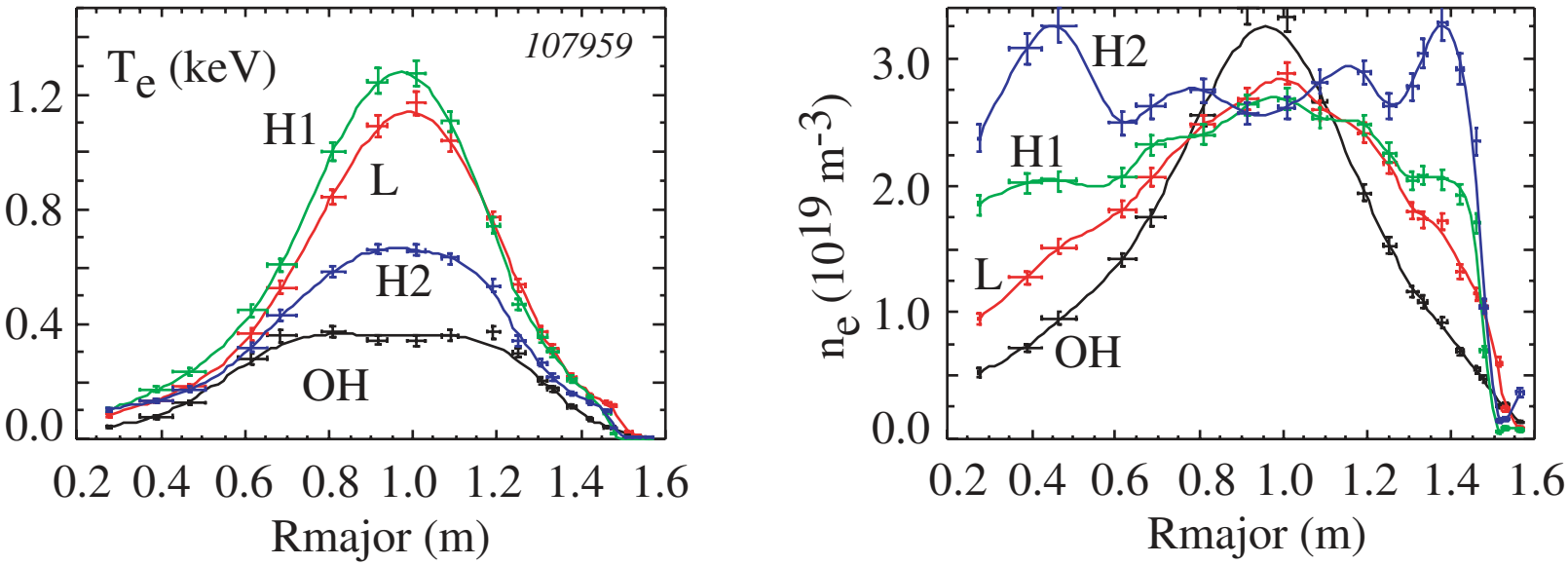
T_e (keV)
107959
H1
L
H2
OH
1.2
0.8
0.4
0.0
0.2 0.4 0.6 0.8 1.0 1.2 1.4 1.6
Rmajor (m)
n_e (10^{19} m^{-3})
H2
H1
L
OH
3.0
2.0
1.0
0.0
0.2 0.4 0.6 0.8 1.0 1.2 1.4 1.6
Rmajor (m)

Fig. 18

External Distribution

Plasma Research Laboratory, Australian National University, Australia
Professor I.R. Jones, Flinders University, Australia
Professor João Canalle, Instituto de Fisica DEQ/IF - UERJ, Brazil
Mr. Gerson O. Ludwig, Instituto Nacional de Pesquisas, Brazil
Dr. P.H. Sakanaka, Instituto Fisica, Brazil
The Librarian, Culham Laboratory, England
Mrs. S.A. Hutchinson, JET Library, England
Professor M.N. Bussac, Ecole Polytechnique, France
Librarian, Max-Planck-Institut für Plasmaphysik, Germany
Jolan Moldvai, Reports Library, MTA KFKI-ATKI, Hungary
Dr. P. Kaw, Institute for Plasma Research, India
Ms. P.J. Pathak, Librarian, Insitute for Plasma Research, India
Ms. Clelia De Palo, Associazione EURATOM-ENEA, Italy
Dr. G. Grosso, Instituto di Fisica del Plasma, Italy
Librarian, Naka Fusion Research Establishment, JAERI, Japan
Library, Plasma Physics Laboratory, Kyoto University, Japan
Research Information Center, National Institute for Fusion Science, Japan
Dr. O. Mitarai, Kyushu Tokai University, Japan
Dr. Jiangang Li, Institute of Plasma Physics, Chinese Academy of Sciences, People's Republic of China
Professor Yuping Huo, School of Physical Science and Technology, People's Republic of China
Library, Academia Sinica, Institute of Plasma Physics, People's Republic of China
Librarian, Institute of Physics, Chinese Academy of Sciences, People's Republic of China
Dr. S. Mirnov, TRINITI, Troitsk, Russian Federation, Russia
Dr. V.S. Strelkov, Kurchatov Institute, Russian Federation, Russia
Professor Peter Lukac, Katedra Fyziky Plazmy MFF UK, Mlynska dolina F-2, Komenskeho Univerzita, SK-842 15 Bratislava, Slovakia
Dr. G.S. Lee, Korea Basic Science Institute, South Korea
Institute for Plasma Research, University of Maryland, USA
Librarian, Fusion Energy Division, Oak Ridge National Laboratory, USA
Librarian, Institute of Fusion Studies, University of Texas, USA
Librarian, Magnetic Fusion Program, Lawrence Livermore National Laboratory, USA
Library, General Atomics, USA
Plasma Physics Group, Fusion Energy Research Program, University of California at San Diego, USA
Plasma Physics Library, Columbia University, USA
Alkesh Punjabi, Center for Fusion Research and Training, Hampton University, USA
Dr. W.M. Stacey, Fusion Research Center, Georgia Institute of Technology, USA
Dr. John Willis, U.S. Department of Energy, Office of Fusion Energy Sciences, USA
Mr. Paul H. Wright, Indianapolis, Indiana, USA

The Princeton Plasma Physics Laboratory is operated
by Princeton University under contract
with the U.S. Department of Energy.

Information Services
Princeton Plasma Physics Laboratory
P.O. Box 451
Princeton, NJ 08543

Phone: 609-243-2750
Fax: 609-243-2751
e-mail: pppl_info@pppl.gov
Internet Address: http://www.pppl.gov